

Exploring Quantum Phases of Dipolar Gases through Quasicrystalline Confinement

Vinicius Zamprônio,^{1,2,*} Alejandro Mendoza-Coto,^{3,4,†} Tommaso Macrì,^{5,1,‡} and Fabio Cinti^{2,6,7,§}

¹*Departamento de Física Teórica e Experimental,*

Universidade Federal do Rio Grande do Norte, 59075-000 Natal, Brazil

²*Dipartimento di Fisica e Astronomia, Università di Firenze, I-50019, Sesto Fiorentino (FI), Italy*

³*Departamento de Física, Universidade Federal de Santa Catarina, 88040-900 Florianópolis, Brazil*

⁴*Max Planck Institute for the Physics of Complex Systems, Nothnitzerstr. 38, 01187 Dresden, Germany*

⁵*ITAMP, Harvard-Smithsonian Center for Astrophysics, Cambridge, Massachusetts 02138, USA*

⁶*INFN, Sezione di Firenze, I-50019, Sesto Fiorentino (FI), Italy*

⁷*Department of Physics, University of Johannesburg,*

P.O. Box 524, Auckland Park 2006, South Africa

The effects of frustration on extended supersolid states is a largely unexplored subject in the realm of cold-atom systems. In this work, we explore the impact of quasicrystalline lattices on the supersolid phases of dipolar bosons. Our findings reveal that weak quasicrystalline lattices can induce a variety of modulated phases, merging the inherent solid pattern with a quasiperiodic decoration induced by the external potential. As the lattice becomes stronger, we observe a super quasicrystal phase and a Bose glass phase. Our results, supported by a detailed discussion on experimental feasibility using dysprosium atoms and quasicrystalline optical lattice potentials, open a new avenue in the exploration of long-range interacting quantum systems in aperiodic environments. We provide a solid foundation for future experimental investigations, potentially confirming our theoretical predictions and contributing profoundly to the field of quantum gases in complex external potentials.

Introduction – The exploration of exotic quantum phases displaying simultaneously different kinds of orders, or *quasi*-orders in systems with long-range interactions, has emerged as a central goal in condensed-matter physics [1]. Among these, electronic liquid crystals [2, 3], Bose glasses (BGs) [4, 5], supersolids [6–9], and quantum systems with quasiperiodic order [10–14] stand out as intriguing manifestations combining translational, rotational, and global gauge symmetry breaking. Such systems exhibit exotic collective behaviors arising from intricate interplays between quantum effects, topology, and interactions, holding promise for applications ranging from quantum simulators to advanced materials [9, 15–21]. In this context, the study of dipolar bosons has garnered increasing interest, driven by advancements in both theoretical [22–33] and experimental [34–44] research.

Recent investigations in these systems revealed a rich phase diagram with three distinct supersolid phases—stripes, triangular, and honeycomb—eventually converging at a critical point [31, 45, 46]. In the conventional scenario, the crystallization transition is expected to be first-order, resulting in a sudden increase in the modulation amplitude upon dynamically crossing the crystallization line. This impacts the phase coherence of the system and leads to the generation of high-energy excitations [47], hindering the stability of the supersolid phase.

Exploring the introduction of disorder into these systems could further open new avenues for understanding pioneering complex phases. In non-interacting 2D models, disorder generates non-trivial effects such as Anderson [48–50] and many-body localization [51]. Moreover,

the presence of contact interactions in disordered Bose systems frustrates localization and leads to the emergence of BG physics [5, 52]. Quasicrystal lattices (QCLs) present intriguing platforms for investigating disorder-induced phenomena, particularly due to the observed phase transition from extended to exponentially-localized states with increasing QCL intensity [5, 49, 53]. In QCL environments, quantum gases with contact interactions exhibit not only the anticipated disordered system effects [54–61], but also the emergence of quasicrystalline superfluids [11]. In the case of long-range interacting dipolar systems an intriguing possibility is the study of frustrated phases resulting from the competition between the natural tendency of the system to form periodic supersolids and the presence of a QCL.

In this letter, we bridge the physics of long-range dipolar bosons with the effects of QCL confinement. By numerically solving extensive Gross-Pitaevskii equations (GPE), we explore the phase diagram of the model guided by a spectral variational study. We observe the emergence of global-ordered phases, whose formation mechanism is triggered by the local disorder generated by the QCL. Importantly, our analysis guides experimental implementations within the scope of current technological capabilities. This approach offers the potential to probe and explore these intriguing phases of matter, significantly enhancing our understanding of quantum systems in complex potentials.

Model and Methods – We consider a gas of N interacting bosons of mass m and dipolar length a_{dd} at $T = 0$. The atoms are harmonically trapped along the polarization axis and subjected to a QCL [55, 56] in the plane perpendicular to the polarization axis. The condensate

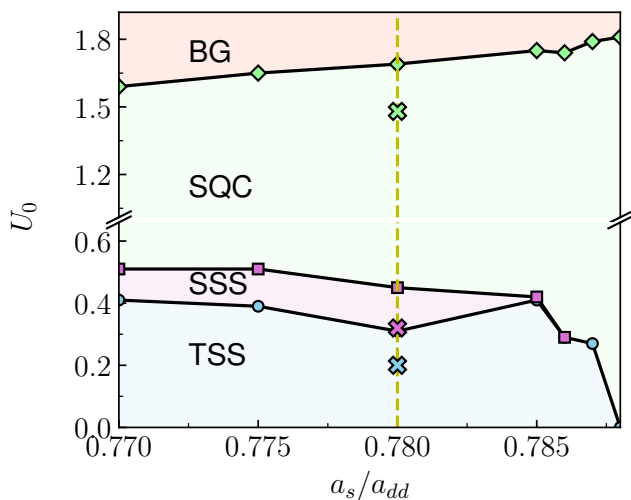


Figure 1. **Phase diagram of dipolar bosons in a quasicrystalline lattice.** We numerically solve Eq. (1) in imaginary time to demonstrate the emergence of several phases induced by the simultaneous effect of a quasicrystalline potential with intensity U_0 and contact (with strength a_s) and dipolar (a_{dd}) interactions. We observe the triangular-supersolid (TSS), stripe-supersolid (SSS), super-quasicrystal (SQC), and Bose glass (BG) phases, as described in the text. For $a_s/a_{dd} \gtrsim 0.79$ and vanishing U_0 , we recover the known limit of SQC. The average scaled density of the effective two-dimensional system is $\bar{\rho}_\perp = 120$, the wave vector of the quasicrystalline modulation is $q = 1.8$, and the frequency of the harmonic trap along the polarization axis is $\omega_z = 0.08$. The vertical dashed line corresponds to the analysis done in Fig. 3. The crosses are representative points of the density patterns in Fig. 2.

wave function, $\psi(\mathbf{r})$, is normalized to unity, hence the local atomic density is given by $\rho(\mathbf{r}) = N|\psi(\mathbf{r})|^2$. Choosing the units of length as $\ell = 12\pi a_{dd}$ and time as $t_0 = m\ell^2/\hbar$, we can express the GPE [62, 63] as

$$i\frac{d\psi(\mathbf{r})}{dt} = \left[-\frac{1}{2}\nabla^2 + U(z) + U_q(\mathbf{r}) + \gamma N^{3/2}|\psi(\mathbf{r})|^3 + \frac{a_s}{3a_{dd}}N|\psi(\mathbf{r})|^2 + \frac{N}{4\pi} \int d\mathbf{r}' V(\mathbf{r} - \mathbf{r}')|\psi(\mathbf{r}')|^2 \right] \psi(\mathbf{r}). \quad (1)$$

The first term on the right-hand side of Eq. (1) pertains to the kinetic energy, while the second term corresponds to the axial trapping potential $U(z) = \omega_z^2 z^2/2$, ω_z being the frequency of the axial trap. The in-plane octagonal QCL is described by $U_q(\mathbf{r}) = \sum_{i=0}^3 U_0(1 - \cos(\mathbf{q}_i \cdot \mathbf{r}))/2$, with characteristic wave vectors $\mathbf{q}_i = q(\cos(i\pi/4), \sin(i\pi/4), 0)$ [64]. The fourth contribution to Eq. (1) corresponds to the Lee-Huang-Yang (LHY) correction to the mean-field approximation [65–67], where

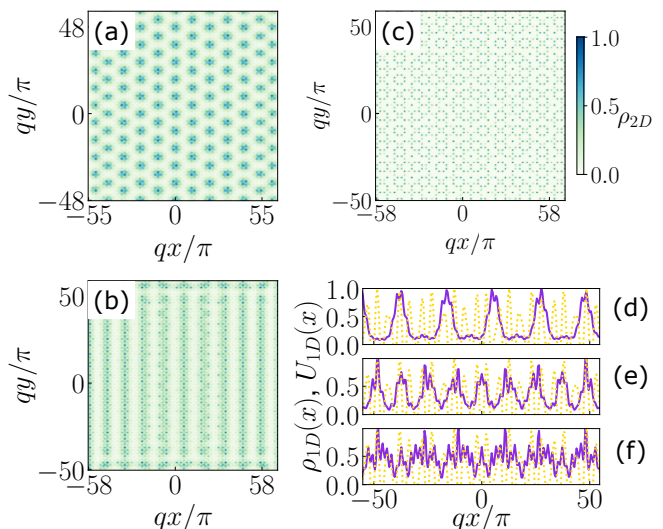


Figure 2. **Normalized density patterns.** (a)-(c) Two-dimensional density $\rho_{2D} = \rho_\perp(x, y)/\rho_\perp^{\max}$ obtained via the numerical solution of Eq. (1). (d)-(f) $\rho_{1D}(x) = \rho_\perp(x, 0)/\rho_\perp^{\max}$ (solid curves) and QCL $U_{1D}(x) = U_q(x, 0)/U_q^{\max}$ (dotted curves), at the $y = 0$ line. The system parameters are the same as in Fig. 1 with $a_s/a_{dd} = 0.78$. In (a, d), the system is in the TSS state with $U_0 = 0.20$. In (b, e), the SSS state is represented for $U_0 = 0.32$. In (c, f), the SQC state is shown for $U_0 = 1.44$. The BG state is visually indistinguishable from the SQC.

$\gamma = \frac{4}{3\pi^2} \left(\frac{a_s}{3a_{dd}}\right)^{5/2} \left[1 + \frac{3}{2} \left(\frac{a_s}{a_{dd}}\right)^2\right]$ [68]. Finally, the last two terms of Eq. (1) account for the scaled contact-interaction, with scattering length a_s , and the dipolar interaction, $V(\mathbf{r}) = (1 - \frac{3z^2}{r^2})\frac{1}{r^3} + \frac{8\pi}{3}\delta(r)$. The ground state ψ_0 of the system is obtained by evolving an initial ansatz $\psi(\mathbf{r}, t = 0)$ in imaginary time. Details about $\psi(\mathbf{r}, t = 0)$ are described in the Supplemental Material [69].

We have also implemented a spectral variational method (SVM), see [69] and [13, 31, 70]. In summary, after introducing the average 2D density of particles $\rho_\perp(\mathbf{r}_\perp) = N \int dz |\psi_0|^2(\mathbf{r})$, an effective energy functional in terms of $\rho_\perp(\mathbf{r}_\perp)$ is constructed and used to study the extended phases of the system. We consider an effective 2D wave function of the form $\psi_\perp = \psi_{\text{dip}} \psi_{\text{oct}}$, where ψ_{dip} represents extended wave functions with $\pi/3$ or π rotational symmetries, and ψ_{oct} corresponds to the quasicrystalline component with octagonal rotational symmetry [69]. The SVM shows that the optimal orientation of the periodic structure of the pattern, described by ψ_{dip} , with respect to one of the main directions of the QCL is $\pi/8$. Such configuration is difficult to implement in the GPE solution considering the constraints imposed by the periodic boundary conditions. However, our analytical study shows that considering two main directions, of the periodic pattern and the QCL, respectively aligned have a safely negligible energy cost, making numerical results with aligned patterns an excellent approximation of

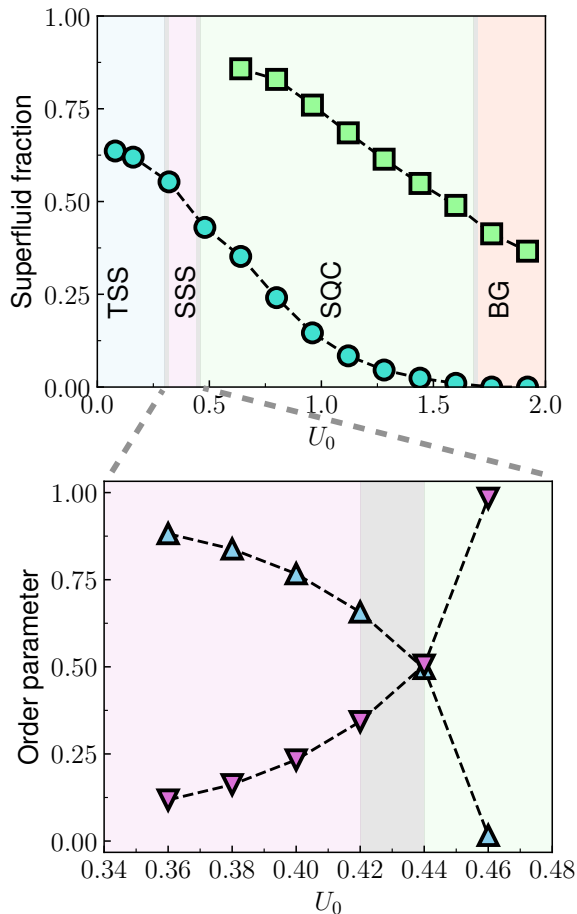


Figure 3. **Characterization of the system ground-state.** We display the global superfluid fraction (circles), the local superfluid fraction (squares), and the stripe-order (triangles) and quasicrystalline-order (upside-down triangles) parameters. The gray regions delimit the phase transitions. The system parameters are the same as in Fig. 2.

the actual ground state of the system [69].

Results. – We numerically solve the GPE considering $\omega_z = 0.08$, average in-plane density $\bar{\rho}_\perp = 120$, and $0.77 \leq a_s/a_{dd} \lesssim 0.79$. The characteristic wave vectors of the QCL have moduli $q = 1.8$, which is about five times the characteristic wave vector k_0 of the triangular supersolid (TSS) found when $U_0 = 0$. As shown in the phase diagram in Fig. 1, which is constructed by tuning the QCL intensity U_0 and the ratio between a_s and a_{dd} , we identify four distinct phases in the regime of parameters considered: a TSS; a stripe supersolid (SSS); a superquasicrystal (SQC), a phase in which the quasicrystalline density pattern coexists with a finite global superfluid fraction; and a Bose glass (BG). Remarkably, for the set of parameters considered, the SSS is never the ground state of the system in the absence of the QCL [45, 46]. Indeed, by increasing the intensity of the high-momentum QCL, we induce a delocalization of the clusters of par-

ticles in the TSS. This makes a transition to the SSS favorable as a mechanism of energy minimization. A similar behavior is already observed in the absence of the QCL when the density of particles is increased [45]. Interestingly, at large U_0 , when the dipolar interaction is not able to sustain the periodic pattern anymore, it then produces a strong repulsion between neighboring clusters which depletes some of the valleys of the QCL generating a quasicrystalline density pattern that does not match the QCL [69].

The phase diagram can be better understood with the help of Fig. 2, where we depict the observed ground-state configurations. For weak QCLs, the ground state corresponds to the TSS state shown in Fig. 2(a). As U_0 is increased, eventually we have a transition to the SSS state, Fig. 2(b). In the intermediate U_0 regime, the stripe ansatz evolves to the SQC state, Fig. 2(c). In Figs. 2(d)-(f), we show the density patterns along the $y = 0$ line. We observe that by increasing the intensity of the QCL in the large q regime ($q \gg k_0$) the system delocalizes. This effect can be attributed to the local disorder that characterizes the lattice. To some extent, stabilization of superfluid clusters and stripes is boosted by a process reminiscent of superfluids caged in puddles, as featured in BG phases [52, 71–75]. Eventually, clusters in the QCL produce an increase of the effective dipolar repulsion triggering the transitions to the SSS and the SQC. As we will see later, for $q \sim k_0$, such a mechanism does not take place since the system is more susceptible to the QCL.

In Fig. 3, we show the behavior of quantities used to characterize the phases of the system and to locate their boundaries in Fig. 1. Additionally, we considered the density contrast to classify solid states [69]. We computed the superfluid fraction considering a generalization of Leggett’s criterion [76],

$$f = \frac{L_x^2 L_y^2}{\int d\mathbf{r}_\perp \rho_\perp(\mathbf{r}_\perp) \int d\mathbf{r}'_\perp \rho_\perp(\mathbf{r}'_\perp)^{-1}}, \quad (2)$$

where $L_{x(y)}$ is the length of the system in the $x(y)$ direction, see Ref. [13]. At strong U_0 , the SQC transitions to the BG whenever $f = 0$. To differentiate between a BG and a Mott insulator, we consider local superfluidity on the first ring of clusters around the origin [77]. Both BG and insulating states have zero global superfluidity, but the former has local superfluidity in some puddles. The local superfluid fraction on a ring of radius R is $f_{\text{loc}} = 4\pi^2 / \int_0^{2\pi} R d\theta \rho_\perp^{-1}(\mathbf{R})$, where $\mathbf{R} = (R \cos \theta, R \sin \theta)$ [78]. See Ref. [69] for additional information on how to locate these rings. In Fig. 3(a), we show the local superfluid fraction in an interval of U_0 where the QCL dominates. We see that it remains finite when the global superfluidity vanishes ($U_0 \gtrsim 1.69$), which indicates that in the strong U_0 regime, the system is a BG.

At intermediate U_0 , we observe a competition between the SSS (TSS) and QCL patterns. To mea-

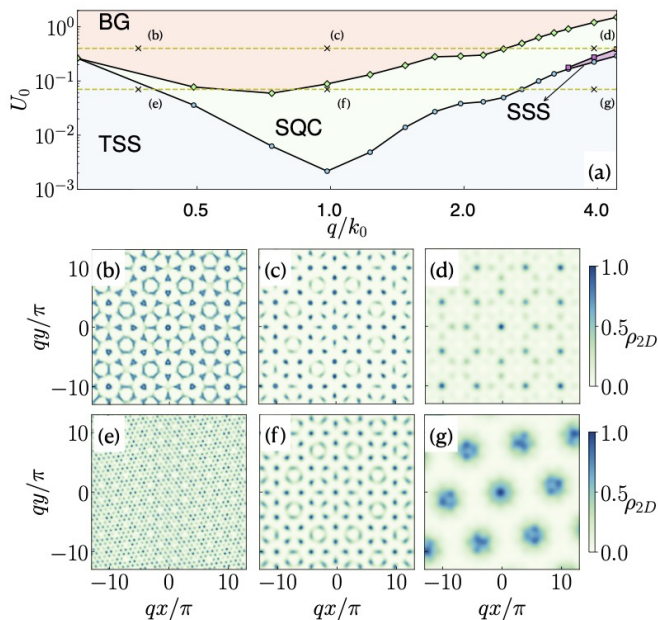


Figure 4. **The phase diagram of q versus U_0 .** (a) is the phase diagram in the U_0 versus q plane, in which we indicate with crosses the positions of the density patterns shown in (b)-(g). All the system parameters, but q , are the same as in Fig. 2. (b)-(d) are three density patterns at $U_0 = 0.40$ and (b) $q = 0.15$, (c) $q = 0.4$, and (d) $q = 1.6$. (e)-(g) are three density patterns at $U_0 = 0.07$ and (e) $q = 0.15$, (f) $q = 0.4$, and (g) $q = 1.6$.

sure how much each of these patterns contributes to the mixed state, we study the Fourier transform of the density $\hat{\rho}_\perp(\mathbf{k}_\perp) \propto \int d\mathbf{r}_\perp \rho_\perp(\mathbf{r}_\perp) e^{i\mathbf{k}_\perp \cdot \mathbf{r}_\perp}$. The SSS (TSS) and QCL patterns have, respectively, two (six) and eight characteristic peaks in the profile of $\hat{\rho}_\perp(\mathbf{k}_\perp)$. Once we measure the average height h of each kind of characteristic peaks, see details in Ref. [69], we estimate the SSS (TSS) composition through the parameters $\Delta_{SSS(TSS)} = h_{SSS(TSS)} / (h_{SSS(TSS)} + h_{SQC})$ and $\Delta_{SQC} = h_{SQC} / (h_{SSS(TSS)} + h_{SQC})$ [79]. The SSS (TSS) to SQC phase transition is thus identified as the lower bound of a phase in which $\Delta_{SQC} > \Delta_{SSS(TSS)}$, see Fig. 3(b).

At weak U_0 , the TSS, SSS and SQC states are metastable states, meaning that the outcome of the imaginary-time evolution is settled by the initial ansatz $\psi(\mathbf{r}, t = 0)$. Therefore, the ground state of the system is the one that provides the smaller energy at the end of the imaginary-time evolution.

The phenomenology discussed so far corresponds to a situation in which the characteristic wave vector $q \gg k_0$. The role of q has been grasped by employing the SVM. Fig. 4(a) depicts the phase diagram by varying q/k_0 and U_0 , keeping both density $\bar{\rho}_\perp$ and a_s/a_{dd} fixed. For $q \sim k_0$, the TSS melts into an SQC due to the competition with the QCL ordering for small values of U_0 . In panels (b)-

(g), we show the ground-state configuration as q increases for two different values of U_0 . As can be noticed, for large U_0 , a crossover between different quasicrystal structures takes place as q is increased resulting from an increase of the dipolar repulsion between cluster localized at the QCL minima. This enhancement of the dipolar repulsion induce the depletion of shallower QCL minima giving place to a quasicrystal with a higher average distance between clusters. For strong U_0 we see that the BG phase surprisingly melts in the superfluid SQC even if increasing q is similar to increasing density. This phenomenology is also observed in contact-interaction systems [58].

Experimental feasibility – The theoretical results presented here are in a regime of parameters well within the current experimental capabilities [36, 38, 47, 80, 81]. We propose a potential experiment using ^{162}Dy atoms. This system offers a wide range of s -wave scattering lengths a_s , with a dipolar length $a_{dd} \approx 7$ nm, which results in a range of a_s/a_{dd} consistent with the values considered in this work. For ^{162}Dy , the characteristic units of length and time are $\ell = 0.26 \mu\text{m}$ and $t_0 = 0.18$ ms. The trapping dimensionless frequency $\omega_z t_0 = 0.08$ is equivalent to $\omega_z \approx 450$ Hz. For $a_s/a_{dd} = 0.77$ and effective two-dimensional density $\bar{\rho}_\perp = 120$, we estimate a condensate thickness $\sigma_z \approx 7.8 \mu\text{m}$ and a peak 3D density in the absence of the QCL $3\rho_\perp/4\sigma_z \approx 1.65 \times 10^{14} \text{ cm}^{-3}$. In these conditions, the ground-state characteristic wave vector of the triangular solid is $k_0 \approx 0.4$, resulting in a lattice spacing $\lambda = 4\pi/(\sqrt{3}k_0) \approx 4.7 \mu\text{m}$, a small enough value to experimentally detect the long-distance properties of the predicted phases.

Recent works have successfully replicated the potential of an octagonal QCL using optical lattices [55, 56]. The experimental setup involves superimposing four coplanar 1D lattices, formed by retroreflective laser beams, arranged at 45° angles relative to each other. We considered QCLs whose characteristic wave vector q approximately varies in the range from $k_0/4$ to $4k_0$, which results in a wavelength interval $\Delta\lambda_q \approx (1.02, 16.3)\mu\text{m}$. For the lattice intensity U_0 , our theoretical parameters also fall into an experimentally feasible region. In [56], the authors use U_0 values up to 4.6 Er (where Er is the recoil energy), equivalent to $U_0 = 1.27$ in our units. This value falls within the BG phase in the phase diagram of Fig. 4.

Conclusions – In this work, we studied the effects of a QCL on the TSS phase exhibited by a planar system of dipolar bosons near the critical point. For weak QCL with high characteristic momentum, the system develops a hexagonal (TSS) or stripe (SSS) pattern decorated with a quasicrystalline structure that simultaneously exhibits global superfluid properties. Interestingly, we observe that the TSS to SSS transition increasing the depth of the QCL occurs as a mechanism to minimize the dipolar repulsion when $q \gg k_0$ (see Fig. 4). Microscopically, increasing the strength of a fast spatially-varying QCL

promotes delocalization on the clusters, which effectively increases the size of the droplets in the TSS and triggers the transition. A further increase of U_0 at the TSS or SSS phases eventually produces a transition to the SQC phase and later to the BG phase. Moreover, by enlarging q we observe that QC phases develop a crossover from a state where the density pattern matches the QCL to a state in which they are different. Finally, the insights from our investigation have laid the foundation for the experimental exploration, enabling us to understand the physics of long-range interacting quantum gases in quasi-periodic geometries.

Acknowledgments: We acknowledge M. Ciardi and Y.-C. Zhang for useful discussions. F. C. and V. Z. acknowledges financial support from PNRR MUR Project No. PE0000023-NQSTI. V. Z. thanks the Instituto Serapilehira for support (grant number Serra-1812- 27802). A.M.C. acknowledge MIPPKS for financial support and hospitality. We thank the High-Performance Computing Center (NPAD) at UFRN for providing computational resources.

* v.zamproniopedroso@unifi.it

† alejandro.mendoza@ufsc.br

‡ tommasomacri@gmail.com

§ fabio.cinti@unifi.it

- [1] N. Defenu, T. Donner, T. Macrì, G. Pagano, S. Ruffo, and A. Trombettoni, Long-range interacting quantum systems, *Rev. Mod. Phys.* **95**, 035002 (2023).
- [2] S. A. Kivelson, E. Fradkin, and V. J. Emery, Electronic liquid-crystal phases of a doped mott insulator, *Nature* **393**, 550 (1998).
- [3] R. M. Fernandes, A. V. Chubukov, and J. Schmalian, What drives nematic order in iron-based superconductors?, *Nature Physics* **10**, 97 (2014).
- [4] R. Yu, L. Yin, N. S. Sullivan, J. S. Xia, C. Huan, A. Paduan-Filho, N. F. O. Jr, S. Haas, A. Steppke, C. F. Miclea, F. Weickert, R. Movshovich, E.-D. Mun, B. L. Scott, V. S. Zapf, and T. Roscilde, Bose glass and mott glass of quasiparticles in a doped quantum magnet, *Nature* **489**, 379 (2012).
- [5] J.-C. Yu, S. Bhave, L. Reeve, B. Song, and U. Schneider, Observing the two-dimensional bose glass in an optical quasicrystal (2023), arXiv:2303.00737 [cond-mat.quant-gas].
- [6] M. Boninsegni and N. V. Prokof'ev, Colloquium: Supersolids: What and where are they?, *Rev. Mod. Phys.* **84**, 759 (2012).
- [7] T. Macrì, F. Maucher, F. Cinti, and T. Pohl, Elementary excitations of ultracold soft-core bosons across the superfluid-supersolid phase transition, *Phys. Rev. A* **87**, 061602 (2013).
- [8] F. Cinti, T. Macrì, W. Lechner, G. Pupillo, and T. Pohl, Defect-induced supersolidity with soft-core bosons, *Nature Communications* **5**, 3235 (2014).
- [9] A. Recati and S. Stringari, Supersolidity in ultracold dipolar gases, *Nature Reviews Physics* 10.1038/s42254-023-00648-2 (2023).
- [10] S. Gopalakrishnan, I. Martin, and E. A. Demler, Quantum quasicrystals of spin-orbit-coupled dipolar bosons, *Phys. Rev. Lett.* **111**, 185304 (2013).
- [11] M. Ciardi, A. Angelone, F. Mezzacapo, and F. Cinti, Quasicrystalline bose glass in the absence of disorder and quasidisorder, *Phys. Rev. Lett.* **131**, 173402 (2023).
- [12] G. Pupillo, P. c. v. Zihlerl, and F. Cinti, Quantum cluster quasicrystals, *Phys. Rev. B* **101**, 134522 (2020).
- [13] A. Mendoza-Coto, R. Turcati, V. Zampronio, R. Díaz-Méndez, T. Macrì, and F. Cinti, Exploring quantum quasicrystal patterns: A variational study, *Phys. Rev. B* **105**, 134521 (2022).
- [14] M. Grossklags, M. Ciardi, V. Zampronio, F. Cinti, and A. Mendoza-Coto, Self-induced bose glass phase in quantum cluster quasicrystals (2023), arXiv:2308.12434 [cond-mat.quant-gas].
- [15] D. Jaksch and P. Zoller, The cold atom hubbard toolbox, *Annals of Physics* **315**, 52 (2005), special Issue.
- [16] A. J. Daley, Quantum computing and quantum simulation with group-ii atoms, *Quantum Information Processing* **10**, 865 (2011).
- [17] D. González-Cuadra, P. R. Grzybowski, A. Dauphin, and M. Lewenstein, Strongly correlated bosons on a dynamical lattice, *Phys. Rev. Lett.* **121**, 090402 (2018).
- [18] F. Schäfer, T. Fukuhara, S. Sugawa, Y. Takasu, and Y. Takahashi, Tools for quantum simulation with ultracold atoms in optical lattices, *Nature Reviews Physics* **2**, 411 (2020).
- [19] F. Cinti, M. Boninsegni, and T. Pohl, Exchange-induced crystallization of soft-core bosons, *New Journal of Physics* **16**, 033038 (2014).
- [20] F. Wächtler and L. Santos, Quantum filaments in dipolar bose-einstein condensates, *Phys. Rev. A* **93**, 061603 (2016).
- [21] F. Wächtler and L. Santos, Ground-state properties and elementary excitations of quantum droplets in dipolar bose-einstein condensates, *Phys. Rev. A* **94**, 043618 (2016).
- [22] T. Lahaye, C. Menotti, L. Santos, M. Lewenstein, and T. Pfau, The physics of dipolar bosonic quantum gases, *Reports on Progress in Physics* **72**, 126401 (2009).
- [23] Z.-K. Lu, Y. Li, D. S. Petrov, and G. V. Shlyapnikov, Stable dilute supersolid of two-dimensional dipolar bosons, *Phys. Rev. Lett.* **115**, 075303 (2015).
- [24] D. Baillie and P. B. Blakie, Droplet crystal ground states of a dipolar bose gas, *Phys. Rev. Lett.* **121**, 195301 (2018).
- [25] H. Saito, Path-integral monte carlo study on a droplet of a dipolar bose-einstein condensate stabilized by quantum fluctuation, *Journal of the Physical Society of Japan* **85**, 053001 (2016).
- [26] F. Cinti, P. Jain, M. Boninsegni, A. Micheli, P. Zoller, and G. Pupillo, Supersolid droplet crystal in a dipole-blockaded gas, *Phys. Rev. Lett.* **105**, 135301 (2010).
- [27] K. Nho and D. P. Landau, Bose-einstein condensation of trapped atoms with dipole interactions, *Phys. Rev. A* **72**, 023615 (2005).
- [28] F. Cinti and M. Boninsegni, Classical and quantum filaments in the ground state of trapped dipolar bose gases, *Phys. Rev. A* **96**, 013627 (2017).
- [29] Y. Kora and M. Boninsegni, Patterned supersolids in dipolar bose systems, *Journal of Low Temperature Physics* **197**, 337 (2019).

- [30] F. Cinti, A. Cappellaro, L. Salasnich, and T. Macrì, Superfluid filaments of dipolar bosons in free space, *Phys. Rev. Lett.* **119**, 215302 (2017).
- [31] Y.-C. Zhang, F. Maucher, and T. Pohl, Supersolidity around a critical point in dipolar bose-einstein condensates, *Phys. Rev. Lett.* **123**, 015301 (2019).
- [32] S. M. Roccuzzo and F. Ancilotto, Supersolid behavior of a dipolar bose-einstein condensate confined in a tube, *Phys. Rev. A* **99**, 041601 (2019).
- [33] M. Ciardi, F. Cinti, G. Pellicane, and S. Prestipino, Supersolid phases of bosonic particles in a bubble trap, *Phys. Rev. Lett.* **132**, 026001 (2024).
- [34] J.-R. Li, J. Lee, W. Huang, S. Burchesky, B. Shteynas, F. Ç. Top, A. O. Jamison, and W. Ketterle, A stripe phase with supersolid properties in spin-orbit-coupled bose-einstein condensates, *Nature* **543**, 91 (2017).
- [35] J. Léonard, A. Morales, P. Zupancic, T. Esslinger, and T. Donner, Supersolid formation in a quantum gas breaking a continuous translational symmetry, *Nature* **543**, 87 (2017).
- [36] L. Tanzi, E. Lucioni, F. Famà, J. Catani, A. Fioretti, C. Gabbanini, R. N. Bisset, L. Santos, and G. Modugno, Observation of a dipolar quantum gas with metastable supersolid properties, *Phys. Rev. Lett.* **122**, 130405 (2019).
- [37] L. Tanzi, S. M. Roccuzzo, E. Lucioni, F. Famà, A. Fioretti, C. Gabbanini, G. Modugno, A. Recati, and S. Stringari, Supersolid symmetry breaking from compressional oscillations in a dipolar quantum gas, *Nature* **574**, 382 (2019).
- [38] F. Böttcher, J.-N. Schmidt, M. Wenzel, J. Hertkorn, M. Guo, T. Langen, and T. Pfau, Transient supersolid properties in an array of dipolar quantum droplets, *Phys. Rev. X* **9**, 011051 (2019).
- [39] L. Chomaz, D. Petter, P. Ilzhöfer, G. Natale, A. Trautmann, C. Politi, G. Durastante, R. M. W. van Bijnen, A. Patscheider, M. Sohmen, M. J. Mark, and F. Ferlaino, Long-lived and transient supersolid behaviors in dipolar quantum gases, *Phys. Rev. X* **9**, 021012 (2019).
- [40] M. Guo, F. Böttcher, J. Hertkorn, J.-N. Schmidt, M. Wenzel, H. P. Büchler, T. Langen, and T. Pfau, The low-energy goldstone mode in a trapped dipolar supersolid, *Nature* **574**, 386 (2019).
- [41] G. Natale, R. M. W. van Bijnen, A. Patscheider, D. Petter, M. J. Mark, L. Chomaz, and F. Ferlaino, Excitation spectrum of a trapped dipolar supersolid and its experimental evidence, *Phys. Rev. Lett.* **123**, 050402 (2019).
- [42] M. A. Norcia, C. Politi, L. Klaus, E. Poli, M. Sohmen, M. J. Mark, R. N. Bisset, L. Santos, and F. Ferlaino, Two-dimensional supersolidity in a dipolar quantum gas, *Nature* **596**, 357 (2021).
- [43] L. Chomaz, I. Ferrier-Barbut, F. Ferlaino, B. Laburthe-Tolra, B. L. Lev, and T. Pfau, Dipolar physics: a review of experiments with magnetic quantum gases, *Reports on Progress in Physics* **86**, 026401 (2022).
- [44] G. Biagioni, N. Antolini, B. Donelli, L. Pezzè, A. Smerzi, M. Fattori, A. Fioretti, C. Gabbanini, M. Inguscio, L. Tanzi, and G. Modugno, Sub-unity superfluid fraction of a supersolid from self-induced josephson effect (2023), arXiv:2311.04757 [cond-mat.quant-gas].
- [45] B. T. E. Ripley, D. Baillie, and P. B. Blakie, Two-dimensional supersolidity in a planar dipolar bose gas, *Phys. Rev. A* **108**, 053321 (2023).
- [46] Y.-C. Zhang, T. Pohl, and F. Maucher, Metastable patterns in one- and two-component dipolar bose-einstein condensates (2023), arXiv:2310.04738 [cond-mat.quant-gas].
- [47] H. Kadau, M. Schmitt, M. Wenzel, C. Wink, T. Maier, I. Ferrier-Barbut, and T. Pfau, Observing the rosenweig instability of a quantum ferrofluid, *Nature* **530**, 194 (2016).
- [48] P. W. Anderson, Absence of diffusion in certain random lattices, *Phys. Rev.* **109**, 1492 (1958).
- [49] G. Roati, C. D'Errico, L. Fallani, M. Fattori, C. Fort, M. Zaccanti, G. Modugno, M. Modugno, and M. Inguscio, Anderson localization of a non-interacting bose-einstein condensate, *Nature* **453**, 895–898 (2008).
- [50] G. Modugno, Anderson localization in bose-einstein condensates, *Reports on Progress in Physics* **73**, 102401 (2010).
- [51] D. A. Abanin, E. Altman, I. Bloch, and M. Serbyn, Colloquium: Many-body localization, thermalization, and entanglement, *Rev. Mod. Phys.* **91**, 021001 (2019).
- [52] M. P. A. Fisher, P. B. Weichman, G. Grinstein, and D. S. Fisher, Boson localization and the superfluid-insulator transition, *Phys. Rev. B* **40**, 546 (1989).
- [53] A. Szabó and U. Schneider, Mixed spectra and partially extended states in a two-dimensional quasiperiodic model, *Phys. Rev. B* **101**, 014205 (2020).
- [54] H. Yao, A. Khoudli, L. Bresque, and L. Sanchez-Palencia, Critical behavior and fractality in shallow one-dimensional quasiperiodic potentials, *Phys. Rev. Lett.* **123**, 070405 (2019).
- [55] K. Viebahn, M. Sbroscia, E. Carter, J.-C. Yu, and U. Schneider, Matter-wave diffraction from a quasicrystalline optical lattice, *Phys. Rev. Lett.* **122**, 110404 (2019).
- [56] M. Sbroscia, K. Viebahn, E. Carter, J.-C. Yu, A. Gaunt, and U. Schneider, Observing localization in a 2d quasicrystalline optical lattice, *Phys. Rev. Lett.* **125**, 200604 (2020).
- [57] H. Yao, T. Giamarchi, and L. Sanchez-Palencia, Lieb-liniger bosons in a shallow quasiperiodic potential: Bose glass phase and fractal mott lobes, *Phys. Rev. Lett.* **125**, 060401 (2020).
- [58] R. Gautier, H. Yao, and L. Sanchez-Palencia, Strongly interacting bosons in a two-dimensional quasicrystal lattice, *Physical Review Letters* **126**, 10.1103/physrevlett.126.110401 (2021).
- [59] M. Ciardi, T. Macrì, and F. Cinti, Finite-temperature phases of trapped bosons in a two-dimensional quasiperiodic potential, *Phys. Rev. A* **105**, L011301 (2022).
- [60] Z. Zhu, S. Yu, D. Johnstone, and L. Sanchez-Palencia, Localization and spectral structure in two-dimensional quasicrystal potentials (2023), arXiv:2307.09527 [cond-mat.quant-gas].
- [61] Z. Zhu, H. Yao, and L. Sanchez-Palencia, Thermodynamic phase diagram of two-dimensional bosons in a quasicrystal potential, *Phys. Rev. Lett.* **130**, 220402 (2023).
- [62] F. Dalfovo, S. Giorgini, L. P. Pitaevskii, and S. Stringari, Theory of bose-einstein condensation in trapped gases, *Rev. Mod. Phys.* **71**, 463 (1999).
- [63] A. J. Leggett, Bose-einstein condensation in the alkali gases: Some fundamental concepts, *Rev. Mod. Phys.* **73**, 307 (2001).
- [64] It is important to notice that due to the presence of the non-local dipolar interaction, different values of the characteristic wave vector q can produce different many-body

- ground-state phases.
- [65] T. D. Lee, K. Huang, and C. N. Yang, Eigenvalues and eigenfunctions of a bose system of hard spheres and its low-temperature properties, *Phys. Rev.* **106**, 1135 (1957).
- [66] T. D. Lee and C. N. Yang, Many-body problem in quantum mechanics and quantum statistical mechanics, *Phys. Rev.* **105**, 1119 (1957).
- [67] D. S. Petrov, Quantum mechanical stabilization of a collapsing bose-bose mixture, *Phys. Rev. Lett.* **115**, 155302 (2015).
- [68] R. N. Bisset, R. M. Wilson, D. Baillie, and P. B. Blakie, Ground-state phase diagram of a dipolar condensate with quantum fluctuations, *Phys. Rev. A* **94**, 033619 (2016).
- [69] V. Zampronio, A. Mendoza-Coto, T. Macrì, and F. Cinti, Supplemental Materials to "Exploring Supersolid Phases in Dipolar Quantum Gases through Quasicrystalline Confinement".
- [70] M. Grossklags, M. Ciardi, V. Zampronio, F. Cinti, and A. Mendoza-Coto, Self-induced bose glass phase in quantum cluster quasicrystals (2023), arXiv:2308.12434 [cond-mat.quant-gas].
- [71] L. Pollet, N. V. Prokof'ev, B. V. Svistunov, and M. Troyer, Absence of a direct superfluid to mott insulator transition in disordered bose systems, *Phys. Rev. Lett.* **103**, 140402 (2009).
- [72] G. Carleo, G. Boéris, M. Holzmann, and L. Sanchez-Palencia, Universal superfluid transition and transport properties of two-dimensional dirty bosons, *Phys. Rev. Lett.* **111**, 050406 (2013).
- [73] i. m. c. G. Söyler, M. Kiselev, N. V. Prokof'ev, and B. V. Svistunov, Phase diagram of the commensurate two-dimensional disordered bose-hubbard model, *Phys. Rev. Lett.* **107**, 185301 (2011).
- [74] M. Ciardi, A. Angelone, F. Mezzacapo, and F. Cinti, Quasicrystalline bose glass in the absence of disorder and quasidisorder, *Phys. Rev. Lett.* **131**, 173402 (2023).
- [75] B. R. de Abreu, F. Cinti, and T. Macrì, Superstripes and quasicrystals in bosonic systems with hard-soft corona interactions, *Phys. Rev. B* **105**, 094505 (2022).
- [76] A. J. Leggett, Can a solid be "superfluid"?, *Phys. Rev. Lett.* **25**, 1543 (1970).
- [77] For f_{loc} to provide meaningful results, we must consider rings containing a finite number of particles.
- [78] K. Furutani and L. Salasnich, Superfluid properties of bright solitons in a ring, *Phys. Rev. A* **105**, 033320 (2022).
- [79] P. M. Chaikin and T. C. Lubensky, *Principles of Condensed Matter Physics* (Cambridge University Press, 1995).
- [80] L. Chomaz, R. M. W. van Bijnen, D. Petter, G. Faraoni, S. Baier, J. H. Becher, M. J. Mark, F. Wächtler, L. Santos, and F. Ferlaino, Observation of roton mode population in a dipolar quantum gas, *Nature Physics* **14**, 442 (2018).
- [81] M. Schmitt, M. Wenzel, F. Böttcher, I. Ferrier-Barbut, and T. Pfau, Self-bound droplets of a dilute magnetic quantum liquid, *Nature* **539**, 259 (2016).

Supplemental Materials: Exploring Supersolid Phases in Dipolar Quantum Gases through Quasicrystalline Confinement

I. NUMERICAL SOLUTION OF THE GPE

In the presence of dipolar interactions and for a weak QCL, several metastable states can be reached during the imaginary-time evolution. Therefore, the global minimum of the energy functional is found after comparing the energies of the stationary states resulting from imaginary-time evolution starting from different initial states. The numerical energy minimization was performed considering a system size consistent with the corresponding initial conditions and using periodic boundary conditions. The optimal solution for each kind of initial condition is found after minimizing the obtained energy concerning the seeded lattice constant a .

We define $\psi(\mathbf{r}, t = 0) = \psi_z(z)\psi_\perp(\mathbf{r}_\perp)$, with $\psi_z(z) \propto \exp[-z^2/(2\sigma_z^2)]$ and

$$\psi_\perp(\mathbf{r}_\perp) \propto \sum_i e^{-\frac{(x-x_i)^2+(y-y_i)^2}{2\sigma_\perp^2}}. \quad (\text{S1})$$

The width of the functions in the sum of Eq. (S1), initially defined by σ_z and σ_\perp , and even their functional form, will evolve as the imaginary-time grows to render the smaller energy associated with a particular choice of the lattice sites (x_i, y_i) . We consider triangular and honeycomb lattices, known to be hexagonal solutions of the ground state of dipolar systems and perform computations with several lattice constants a for each lattice. Additionally, we also consider a stripe ansatz $\psi_\perp(\mathbf{r}_\perp) \propto \exp[-\sum_i x_i^2/(2\sigma_\perp^2)]$, with $x_{i+1} - x_i = a$, and an homogeneous ansatz $\psi_\perp(\mathbf{r}_\perp) \propto 1$.

II. EFFECTIVE 2D ENERGY FUNCTIONAL AND VARIATIONAL ANSÄTZE

The energy functional of the quasi-2D system is

$$\frac{E[\psi]}{N} = \int d\mathbf{r} \left\{ \frac{1}{2} |\nabla \psi(\mathbf{r})|^2 + U(z) |\psi(\mathbf{r})|^2 + U_q(\mathbf{r}) |\psi(\mathbf{r})|^2 + \frac{2}{5} \gamma N^{3/2} |\psi(\mathbf{r})|^5 + N \frac{a_s}{6a_{dd}} |\psi(\mathbf{r})|^4 \right. \\ \left. + \frac{N}{8\pi} \int d\mathbf{r}' V(\mathbf{r} - \mathbf{r}') |\psi(\mathbf{r})|^2 |\psi(\mathbf{r}')|^2 \right\}. \quad (\text{S2})$$

With the Thomas-Fermi approximation for the z component of the wave function, $\psi_0(z) = \sqrt{\frac{3}{4\sigma} \left(1 - \frac{z^2}{\sigma^2}\right)}$, we can now integrate Eq. (S2) over the z -direction to obtain the 2D-projected energy-functional per particle, in terms of the in-plane wave function $\psi_\perp(\mathbf{r}_\perp)$. Up to constant background contribution, this functional reads

$$\frac{\Delta E}{N} = \int \frac{d\mathbf{r}}{A} \left\{ \frac{1}{2} |\nabla \psi_\perp(\mathbf{r})|^2 + U_q(\mathbf{r}) |\psi_\perp(\mathbf{r})|^2 + \frac{9\sqrt{3}\pi}{256\sigma^{3/2}} \gamma \rho^{3/2} |\psi_\perp(\mathbf{r})|^5 + \frac{a_s}{10a_{dd}\sigma} \rho |\psi_\perp(\mathbf{r})|^4 \right. \\ \left. + \frac{\rho}{2} \int d\mathbf{r}' V_{\text{eff}}(\mathbf{r} - \mathbf{r}') |\psi_\perp(\mathbf{r})|^2 |\psi_\perp(\mathbf{r}')|^2 \right\}. \quad (\text{S3})$$

Where we omit the perpendicular symbol in all 2D position vectors to avoid a heavy notation. The effective interaction $V_{\text{eff}}(\mathbf{r})$ produced by the dipolar interaction is such that it writes in momentum space as $\hat{V}_{\text{eff}}(k) = f(k\sigma)/\sigma$ where $f(x) = 3/4\{[3 - 3x^2 + 2x^3 - 3(1+x)^2 \exp(-2x)]/x^5 - 4/15\}$.

The density configurations obtained from GPE (Fig.2) suggests a ground state wave function in which the periodic pattern envelopes the fast-varying quasiperiodic component of the wave function induced by the external lattice. In this way, we propose $\psi_\perp(\mathbf{r}) = \psi_{\text{dip}}(\mathbf{r})\psi_{\text{oct}}(\mathbf{r})$, where

$$\psi_{\text{dip}}(\mathbf{r}) = \frac{1 + \sum_{j \neq 0} c_j \cos(\mathbf{k}_j \cdot \mathbf{r})/2}{\sqrt{1 + \frac{1}{4} \sum_{j \neq 0} c_j^2}}, \quad (\text{S4})$$

$$\psi_{\text{oct}}(\mathbf{r}) = \frac{1 + \sum_{j \neq 0} b_j \cos(\mathbf{q}_j \cdot \mathbf{r})/2}{\sqrt{1 + \frac{1}{4} \sum_{j \neq 0} b_j^2}}. \quad (\text{S5})$$

Here $\{c_j, \mathbf{k}_j\}$ ($\{b_j, \mathbf{q}_j\}$) represent the Fourier amplitudes and corresponding momenta of the periodic (quasiperiodic) component of the wave function. To ensure the expected symmetry properties of $\psi_{\text{dip}}(\mathbf{r})$ and $\psi_{\text{oct}}(\mathbf{r})$, Fourier amplitudes c_j 's or b_j 's corresponding to wave vectors equivalent by symmetry operations of the respective component of the wave function are imposed to be equal. The resulting set of independent Fourier amplitudes as well as the lattice size k_0 of the momentum set $\{\mathbf{k}_j\}$ are variationally determined. On the other hand, the "fractal" set of wave vectors $\{\mathbf{q}_j\}$ is generated from the basis induced by the quasiperiodic octogonal external potential whose characteristic momentum is q . In general, we should admit any possible orientation of the periodic component of the wave function concerning the external quasiperiodic lattice. To account for such degree of freedom we include an arbitrary orientation angle θ of the basis of the set $\{\mathbf{k}_j\}$, measured with respect to the vector $\mathbf{q}_1 = q(1,0)$ imposed by the external potential. Naturally, the value of θ is determined variationally in our energy minimization process. To summarize the properties discussed so far, in Table 1 we present the basis wave vectors employed in the Fourier expansion of each component of the wave function.

For calculations, the set of Fourier modes $\{c_j, \mathbf{k}_j\}$ is truncated at the fifth shell of the lattice, which is enough to observe convergence in the region of parameters investigated. Additionally, the set of wave vectors $\{\mathbf{q}_j\}$ is determined considering all combinations of up to five characteristic vectors of the quasiperiodic potential, which renders 52 independent Fourier coefficients for the expansion of $\psi_{\text{oct}}(\mathbf{r})$. Finally, we verify upon minimization of the energy per particle for each kind of solution that $\theta = \pi/8$ corresponds to the optimal configuration for both the TSS and SSS patterns. However, the dependence of the energy per particle with θ is extremely weak in the regime of parameters explored.

The obtained U_0 versus a_s/a_{dd} phase diagram using the previously discussed spectral variational method is shown in Fig.(S1). We considered a QCL with $q = 1.8$ and an average 2D density of particles $\bar{\rho}_\perp = 120$. The obtained

Wave function component	Basis vector $\mathbf{k}_{0,j}$	Index range
ψ_{dip} (TSS)	$k_0(\cos(\frac{2\pi j}{6} + \theta), \sin(\frac{2\pi j}{6} + \theta))$	$j = 0, 1$
ψ_{dip} (SSS)	$k_0(\cos(\theta), \sin(\theta))$	
ψ_{oct}	$q(\cos \frac{2\pi j}{8}, \sin \frac{2\pi j}{8})$	$j = 0, \dots, 3$

Table I. Components of the wave function for the different phases observed and their respective basis vectors

phase diagram coincides qualitatively with the one shown in Fig.(1). The small deviations observed are expected to be produced by to the differences in the working model, i.e. the analytical work was done using a 2D effective model. Additionally, the variational approach implemented is also limited by the particular ansätze considered for the different phases as well as the GPE is also affected by finite size effects.

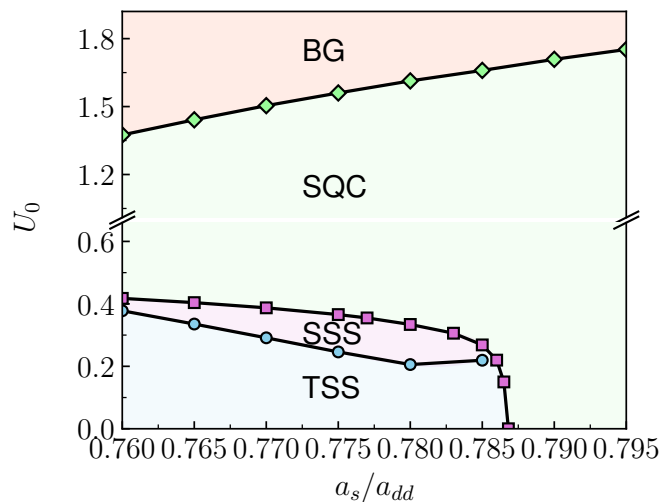


Figure S1. Phase diagram for dipolar bosons in an external quasiperiodic lattice with $q = 1.8$, varying a_s/a_{dd} and U_0 at a fixed average planar density $\bar{\rho}_\perp = 120$. The diagram was calculated through the spectral variational method described above. As in Fig.1 we detect the TSS, SSS, SQC and BG phases.

III. ENERGY COST OF THE RELATIVE ORIENTATION OF SSS AND QCL

As mentioned previously the variational spectral method implemented considers an arbitrary orientation of the TSS and SSS with respect to the QCL. Such orientation is parameterized via the angle θ previously defined. Our variational study lead us to the conclusion that the optimal orientation of both phases is reached for $\theta = \pi/8$. We note that such a configuration would be difficult to implement in the GPE solution due to the periodic boundary conditions. To study the impact of setting $\theta = 0$, as is the GPE, we calculate the relative energy per particle difference $[\epsilon(\theta) - \epsilon(0)]/\epsilon(0)$ for a typical configuration withing the SSS phase. The results are presented in Fig (S2), as we can observe the relative error in such approximation is of order 10^{-6} . Such a small impact on the energy cost of the SSS and TSS implies that in this regard the GPE in the regime of parameters considered are unaffected by the approximation of setting $\theta = 0$.

IV. SQC PATTERN DIFFERENT FROM THE EXTERNAL LATTICE

In Fig. S3 we show the QCL and the density pattern of the SQC in Fig. 2(c). We see that not all the minima of the QCL are populated. This is a mechanism to minimize the dipolar repulsion in the ground state when $q \gg k_0$.

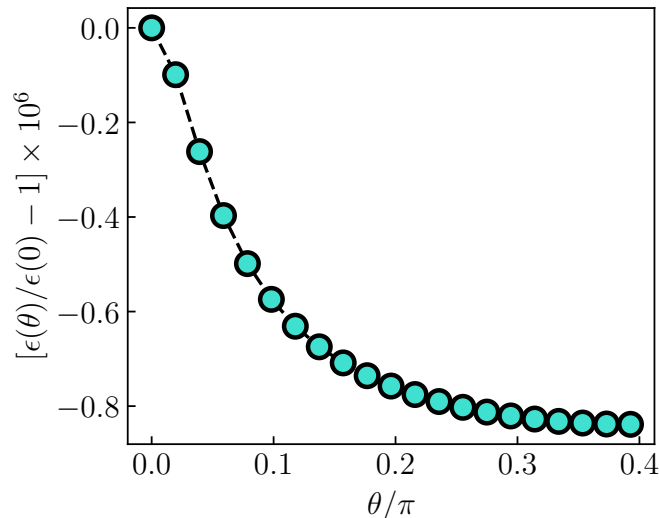


Figure S2. Angular dependence of the energy per particle of the SSS phase varying the orientation of the stripes pattern with respect to one of the main directions of the QC lattice. Results were obtained through the variational spectral method considering the parameters $U_0 = 0.25$, $q = 1.8$ $a_s/a_{dd} = 0.78$ and $\rho_{\perp} = 120$.

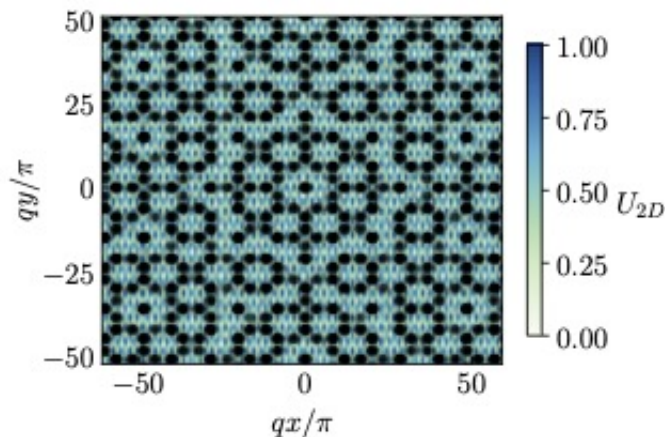


Figure S3. **SQC versus QCL**. The black dots represent the normalized density pattern of the SQC shown in Fig. 2(c). Notice that not all the minima of the QCL $U_{2D} = (U_q - U_q^{\min}) / (U_q^{\max} - U_q^{\min})$ are populated.

V. CONTRAST

The contrast is defined as $\mathcal{C} = (n_{\max} - n_{\min}) / (n_{\max} + n_{\min})$, with $n_{\max(\min)}$ being the maximum (minimum) value of $\rho_{\perp}(\mathbf{r}_{\perp})$. In Fig. S4, we obtained finite values of \mathcal{C} , ruling out the existence of a homogeneous liquid phase in the regimes we considered in Fig. 3 of the main text.

VI. LOCATING RINGS WITH A FINITE DENSITY OF PARTICLES

To locate the rings where local superfluidity is considered, we compute $n_{\circ}(R) = \int d\theta \rho_{\perp}(\mathbf{R}) / 2\pi$, with $\mathbf{R} = R(\cos \theta, \sin \theta)$. Results for this quantity are shown in Fig. S5, where we considered $a_s/a_{dd} = 0.78$ and $U_0 = 0.56$. We see that the first ring around the origin is located at $R \sim 6$, a value that does not change in the regime of a_s/a_{dd} we have considered.

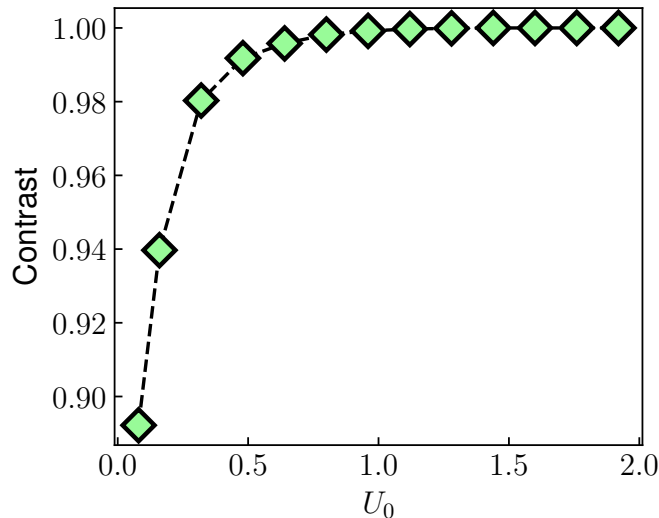


Figure S4. Density contrast as a function of U_0 for $\bar{\rho}_\perp = 120$, $a_s/a_{dd} = 0.78$, $\omega_z = 0.08$ and $q = 1.8$.

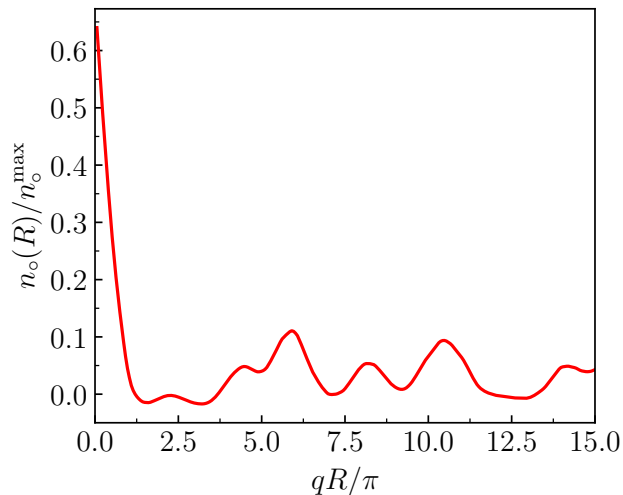


Figure S5. The average number of dipolar bosons in rings of radius R . The average on-plane density is $\bar{\rho}_\perp = 120$, the ratio $a_s/a_{dd} = 0.78$ and $U_0 = 0.56$.

VII. LOCATING AND MEASURING THE PEAKS OF $\tilde{\rho}_\perp(\mathbf{k}_\perp)$

In Fig. S6(a), we show the density profile in reciprocal space for situations where the quasiperiodic pattern dominates. The octagons shown have different sizes and orientations, therefore we devise a procedure to locate and measure the height of the most intense peaks.

We compute the angle-averaged density in momentum space $n_o(k) = \int d\theta \tilde{\rho}_\perp(\mathbf{k})/2\pi$, with $\mathbf{k} = k(\cos\theta, \sin\theta)$, which is shown in Fig. S6(b). We see that peaks appear in the neighborhoods of $k = k_0$ and $k = q$, which are related to the characteristic modulation of the SSS (TSS) and SQC patterns respectively. Then, we locate the peaks $k = k_{\text{peaks}}$ of the circumference circumscribing structures with two (SSS), six (TSS), or eight (SQC) peaks, and we search for the structure that fits our data the best. To do so, we compute

$$S_m(k_{\text{peaks}}, \theta_0) = \sum_{\mathbf{k}_{\text{peaks}}} \tilde{\rho}_\perp(\mathbf{k}_{\text{peaks}}), \quad (\text{S6})$$

with $\mathbf{k}_{\text{peaks}} = k_{\text{peaks}}(\cos\theta, \sin\theta)$, $\theta = \theta_0 + n\pi/m$, n being an integer in the interval $[0, m[$, and $m = 2, 6$, and 8

respectively for the SSS, TSS and SQC states. We span over several values of θ_0 to consider many possible orientations of each structure. The best fit to our data provides the maximum value S_m^{\max} , therefore the height of the peaks can be computed as $h = S_m^{\max}/m$.

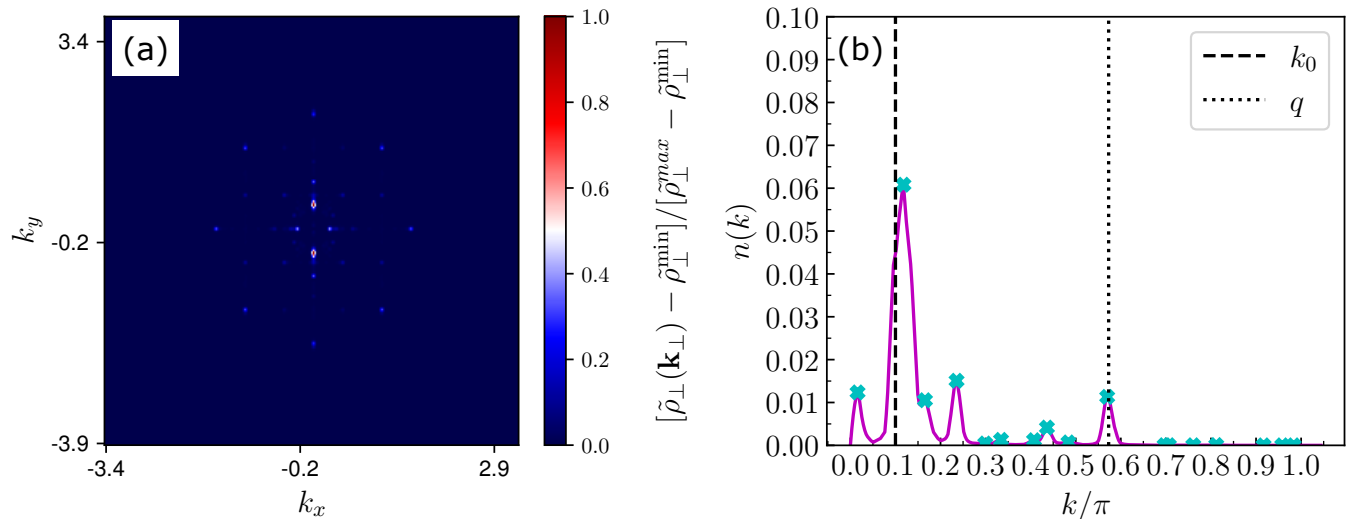


Figure S6. (a) Density pattern in reciprocal space and (b) angle averaged density in the reciprocal space. In $k = k_0$, we have the characteristic momentum of the stripes due to the dipolar interaction ($k_0 = 2\pi/a \approx 0.3$). In $k = q = 1.8$, we have the characteristic momentum of the underlying quasiperiodic lattice. The peak at $k = 0$ was removed. The system parameters are $\omega_z = 0.08$, $\bar{\rho}_\perp = 120$, the ratio $a_s/a_{dd} = 0.78$ and $U_0 = 0.42$. Peaks were found at $k = 0.05, 0.31, 0.53, 0.74, 1.04, 1.28, 1.37, 1.79, 2.40, 2.55, 2.88, \text{ and } 3.09$.

VIII. FOURIER COMPONENTS OF THE QC PHASE

In this section, we present some details of a typical QC configuration obtained by using the SVM. Although we have considered a large Fourier basis for the QC pattern we observed that only a few Fourier modes are activated by the system. To illustrate this fact, we present the results for the five more relevant Fourier modes of a typical configuration within the QC phase for $q = 1.6$ and $\rho_\perp = 120$. It can be verified that as observed in Fig.S6 the wave vectors corresponding to the three most relevant modes are approximately located at $q, 0.765q$, and $0.414q$.

Structure Factor QC, $U_0 = 1.2$, $a_s/a_{dd} = 0.77$, $\rho_\perp = 120$, $q = 1.6$					
Momentum Modulus ($ q $)	1.000	0.765	0.414	1.414	1.082
Momentum Orientation (θ)	0	$\pi/8$	0	0	$\pi/8$
Amplitudes ($\hat{\rho}(\vec{q})$)	0.382	0.244	0.174	0.077	0.035

Table II. Main Fourier components of the normalized QC density pattern. Momenta are expressed in units of the characteristic momentum of the external lattice q . The momentum orientation is relative to the x axis.